RSC Advances

ROYAL SOCIETY OF CHEMISTRY

PAPER

View Article Online
View Journal | View Issue

Cite this: *RSC Adv.*, 2024, **14**, 32436

Construction of Cnts/calcined Zn-Co-LDHs hydrid to enhanced photocatalytic for ofloxacin decomposition: mechanism, degradation pathway, and toxicity assessment†

Nguyen Hoai Nam,[a] Nguyen Quoc Hung,[b] Nguyen Thi Hong Anh,[c]
Nguyen Quoc Thang[a] and Nguyen Thi Mai Tho*[a]

Received 25th August 2024
Accepted 27th September 2024

DOI: 10.1039/d4ra06153e

rsc.li/rsc-advances

This work successfully synthesized the Cnts/calcined Zn-Co-LDHs (xCnts@ZnC) hybrid material using the Zn-Co-LDHs precursor. Using the co-precipitation method, we synthesized Zn-Co-LDHs onto Cnts ranging in mass from 0 to 80 mg. These were subsequently calcined at 550 °C to yield xCnts@ZnC (x = 2, 4, 6, 8). Based on the results, ZnC is found on the surface of Cnts in two phases: ZnO and $ZnCo_2O_4$. The photocatalytic activity of xCnts@ZnC is demonstrated by its capacity to degrade ofloxacin antibiotics (OFL) in the visible region; 6Cnts@ZnC (85.8%; $k = 0.0099$ min^{-1}), shows the best decomposition rate constant, increasing by three times when compared to ZnC (53.3%; $k = 0.0048$ min^{-1}). The h^+, $O_2^{\bullet-}$, radicals are the main factors that determine of the decomposition process in the identified OFL decomposition mechanism of 6Cnts@ZnC, in which Cnts have the role of transporting and collecting electrons, minimizing the recombination between photogenerated electrons and holes. The OFL degradation pathways of 6Cnts@ZnC were also investigated and identified by the HPLC-MS spectrum and suggested the new degradation mechanism to small molecules that have nontoxic of small molecules to environment site by ADMET model. The OFL degradation obtained 96.44% and set equivalent of degradation after completing 300 min.

1 Introduction

The development of antibiotics is a significant milestone in the field of medicine due to their potent antibacterial capabilities, which are effective in the treatment and prevention of infections, inflammation, and other related conditions.[1–3] OFL is one of the fluoroquinolone groups of antibiotics that is typically utilized in both commercial animal treatment and human medicine.[4] The chemical stability of OFL and antibiotics in general means that they frequently do not completely absorb into the bodies of humans or animals. Instead, they are discharged into the environment, contaminating water sources, disrupting the ecological balance, and impacting organisms, so potentially fostering the emergence of antibiotic-resistant bacteria.[5,6] As a result, they are discharged into the environment, contaminating water sources, disrupting the ecological balance, and impacting organisms, so potentially fostering the emergence of antibiotic-resistant bacteria occurrence and removal of multiple.[2,7] Hence, the evaluation and removal of antibiotics from the environment of water has drawn a lot of interest in recent years.[2,8] Environmental technology has examined multiple research approaches for eliminating antibiotics, such as adsorption,[4] photocatalysis, biodegradation,[7] and chemical decomposition.[8] Using advanced oxidation processes (AOPs) is a promising method to break down antibiotics.[9] This method utilizes semiconductors that absorb light in the visible area to generate pairs of electrons (e^-) and holes (h^+), which then remove antibiotics.[10] Mixed metal oxides (MMO) generated from Layered Double Hydroxides (LDHs) have garnered interest recently due to their versatility and simple synthesis.[11,12] The general formula for the layer structure of LDHs is $[M_{1-x}{}^{2+}\,M_x{}^{3+}\,(OH)_2]^{x+}\,(A^{n-})_{x/n}\cdot yH_2O$, where M^{2+} and M^{3+} are the divalent and trivalent metals, respectively, and A^{n-} are the interlayer anions.[12,13] The MMO is composed of a divalent metal oxide and a spinel phase that is generated when LDHs are heated at high temperatures.[14,15] MMO are used for many fields because of their surface adsorption, interlayer anion exchange, and "memory effect" rebuilding of a calcined LDHs precursor.[15–17] Good electrical conductivity is a crucial characteristic of nanocarbons, which come in a variety of

---

[a] Faculty of Chemical Engineering, Industrial University of Ho Chi Minh City, Ho Chi Minh, Vietnam, nguyenthimaitho@iuh.edu.vn

[b] Center of Analytical Services and Experimentation HCM City, 2 Nguyen Van Thu, Đakao, District 1, Ho Chi Minh City, Vietnam

[c] Faculty of Chemical Engineering, Ho Chi Minh City University of Industry and Trade, 140 Le Trong Tan Street, Tay Thanh Ward, Tan Phu District, Ho Chi Minh, Vietnam

† Electronic supplementary information (ESI) available. See DOI: https://doi.org/10.1039/d4ra06153e

allotropes with a wide surface area dispersion, including graphite,[18] graphene (GO),[19] carbon nano tubes (Cnts)[13] and reduced graphene oxide (RGO).[20] To increase the band gap, prevent the combining of photogenerated electrons and holes, and enhance the effectiveness of photocatalysis, in order research has used a hybrid material consisting of MMO and nanocarbons.[21,22] Several specific investigations, including RGO/Ni-Fe-MMO,[20] GO/Zn-Al-MMO,[14] Cnts/Zn-Cr-MMO,[13] and RGO/Zn-Bi-MMO,[23] have successfully used this graft material as a photocatalyst for the degradation of dyes or antibiotics. Motivated by the advantages MMO with LDHs precursors and nanocarbons, especially Cnts, we researched the synthesis of Cnts@Zn-Co-MMO hybrid material and applied the decomposition of OFL antibiotics in the visible light. The effects of various parameters on the photodegradation of OFL were investigated and discussed in detail. Furthermore, the photocatalyst's degradation mechanism was identified, and a new OFL degradation mechanism was projected.

One modern economic trend is the use of computational approaches for drug design and property forecasting. There is a relationship between environmental characteristics and drug design models, but these parameters are also environmental. Pharmacy technicians, chemists, and environmental chemists can evaluate the toxicity of drugs and the environment using multiple models, one of which is the ADMET model.[24–26] Some model predicted well ADMET of active compound *in vitro* likeness drug.[27,28] The environmental impact for intermediate products of OFL degradation was assessed in this study using the ADMET prediction model.

2 Materials and methods

2.1 Materials

Cobalt(II) nitrate hexahydrate ($Co(NO_3)_2\cdot 6H_2O$; 98%), zinc acetate dihydrate ($Zn(CH_3COO)_2\cdot 2H_2O$; 99.5%), ethanol (C_2H_5OH; 99.5%), sodium hydroxide (NaOH; 99%) were purchased from Sigma-Aldrich, USA. Ofloxacin (98%), silver nitrate ($AgNO_3$; 99.8%), ethanol (98%), *p*-benzoquinone (99%), Na_2-EDTA, and were obtained from Xilong Scientific Co., Ltd, China. Carbon nanotubes (Cnts, 99%) were purchased from Jiangsu Xfnano Materials Tech Co., Ltd China.

2.2 Synthesis of *x*Cnts@ZnC hydrid

The *x*Cnts@ZnC photocatalysts were synthesized using the co-precipitation method established by K. M. Parida[29] with different amounts of Cnts ranging from 0 to 80 mg. Solution A contains 100 mL of 0.3 M $Zn(CH_3COO)_2$ and 100 mL of 0.1 M $Co(NO_3)_2$ in the molar ratio Zn/Co 3/1. In mixture B, the Cnts are distributed uniformly in 100 mL of 0.5 M NaOH solution by ultrasonic waves, based on the various masses of Cnts (0, 20, 40, 60, 80 mg). Slowly add solution A into mixture B, resulting in the formation of a pink precipitate in mixture B. The mixture is constantly stirred and maintained at a pH of 10 using a NaOH solution throughout the synthesis process. The pink mixture solution was subjected to thermal aging at 100 °C for 24 hours. The *x*Cnts@ZnC ($x = 0, 2, 4, 6, 8$), the black product, is obtained by drying the product at 100 °C and calcining it at 500 °C for 4 hours. The samples are labeled as follows: ZnC; 2Cnts@ZnC, 4Cnts@ZnC, 6Cnts@ZnC and 8Cnts@ZnC.

2.3 Photocatalytic measurements

The photocatalytic activity of the *x*Cnts@ZnC hydrid were evaluated by analyzing the degradation of OFL in a water solvent under the region of visible light. The suspension consisted of 100 mL of 20 ppm OFL solution and 0.1 g 6Cnts@ZnC was sonicated for 10 minutes and stirred for 50 minutes in dark to reach equilibrium or adsorption. The concentration of OFL (C_o) was subsequently determined.

The photocatalytic system is then exposed directly to the visible light source from the halogen lamp (64640 HLX 150W, 24V, Osram, Germany) for 240 minutes, the maximum intensity of the light source is 100 mW cm^{-2}. Every 30 minutes during the photocatalytic process, 3 mL of the suspension was removed and filtered through a 0.22 μm filter to get away of the solid residues. The decrease in OFL concentration over time was measured using UV spectroscopy at a wavelength of 275 nm. The OFL is directly photolyzed in the absence of a catalyst under the same conditions.

The optimum settings for the catalytic process were determined by analyzing factors influencing the OFL decomposition process of *x*Cnts@ZnC materials, including *x*Cnts@ZnC with different mass of Cnts; initial OFL concentration; the amount of hybrid material and pH. Using HPLC-MS spectrum to identify intermediate products OFL degradation.

3 Results and discussion

3.1 Characterization

3.1.1 XRD & IR. The structure and crystal phase composition of ZnC; Cnts and *x*Cnts@ZnC catalysts were examined using the X-ray diffraction method. The XRD patterns were scanned at diffraction angles ranging from 10° to 80° using monochromatized CuKα radiation ($k = 1.5418$ Å) on D8 Bruker. The XRD results indicate that the ZnC sample shows peaks at angles $2\theta = 31.77°$, 34.44°, 36.45°, 47.61°, 56.61°, 65.13°, 68.12°, 69.11°, 77.03°, which match the crystal planes of ZnO (JCPDS no. 36-1451).[30] Additionally, the peaks at angles $2\theta = 31.509°$, 36.861°, 38.458°, 44.705°, 59.11°, 63.95° correspond to the lattice constants of $ZnCo_2O_4$ (JCPDS 23-1390).[31] The XRD analysis reveals the diffraction patterns of the ZnC sample match research on the characteristics of cLDHs materials. Investigations by Guoqing Zhao on NiFe-LDHs materials obtained by co-precipitation (Bi/Fe = 3/1) after 600 °C heating resulted in NiO and $NiFe_2O_4$.[20] The Cnts sample shows a single peak at the scanning angle $2\theta = 26°$, which is a sign of Cnts (JCPDS 41-1487).[32] The 2Cnts@ZnC, 4Cnts@ZnC, 6Cnts@ZnC and 8Cnts@ZnC hybrid samples have not shown the Cnts peaks to emerge when ZnC is precipitated onto Cnts with varying weight. The reason for this is that the dosage of Cnts is too low, hence the peak intensity of Cnts is too low in comparison to the strength of the peaks of ZnO and $ZnCo_2O_4$ (Fig. 1).[32,33]

The FT-IR (Bruker-EQUINOX) study of the ZnC; 2Cnts@ZnC, 4Cnts@ZnC, 6Cnts@ZnC, and 8Cnts@ZnC samples show peaks at positions 3440 and 1600 cm^{-1}, which correspond to the stretching vibrations of the O–H group in H_2O[20] (Fig. 2A). Additionally, there are peaks observed at locations 800–500 cm^{-1}, which can be attributed to the vibrations of the Co–O and Zn–O groups.[34,35] The 2Cnts@ZnC, 4Cnts@ZnC, 6Cnts@ZnC and 8Cnts@ZnC samples show characteristic vibrations of the C=C bond and vibrations of the C=O bond of COOH group, in along with peaks in the areas 1731–1635 cm^{-1}.[36] The peaks observed between 2964 and 2834 cm^{-1} can be attributed to the stretching vibrations of the C–H bonds in the CH_2 group.[37] This result is also in accordance with the bond structure of Cnts, which includes both C=C; C=O and C–H bonds.

3.1.2 UV-vis DRS &PL. Fig. 2B presents the UV-vis Diffuse Reflectance Spectroscopy (UV-vis DRS) results of Cnts, ZnC, and *x*Cnt@ZnC sample. The Cnts exhibit high absorption over the ultraviolet to visible spectrum. Two distinct absorption edges are evident in the ZnC sample at 386 nm, which corresponds to the ZnO phase, and at 615 nm, which corresponds to $ZnCo_2O_4$. The XRD spectrum analysis of ZnC material, including the two phases ZnO and $ZnCo_2O_4$, is consistent with this conclusion. The absorption edges of Cnts@ZnC exhibit a red shift relative to the absorption edge of ZnC, resulting in a significant extension of the absorption spectrum from the ultraviolet area to the visible region.[36,38,39] The combination of ZnO and $ZnCo_2O_4$ with Cnts has a positive synergistic effect,[40] promoting the transfer of charges from the valence band of ZnC to Cnts.[41] The outcome diminished the recombination process between photogenerated electrons and holes, hence boosting the photocatalytic capacity of *x*Cnts@ZnC.

The material's photocatalytic effectiveness is mostly dependent on the process of recombination between charge transfer and photogenerated electron–holes following light absorption.[42,43] Fig. 2D displays the photoluminescence (PL) measurement outcomes for two samples, ZnC and 6Cnts@ZnC, when excited with a wavelength of 260 nm. The PL data for the ZnC sample reveal a very high maximum peak intensity, indicating a quick recombination rate, resulting in a low photocatalytic efficiency.[44] But with the 6Cnts@ZnC sample, the maximum peak intensity is much lower, which lowers the rate at which photogenerated electrons and holes recombine.[43] This makes it easier for electrons on the ZnC surface to transfer electrons to Cnts, which oxidizes and breaks down antibiotics, boosting the photocatalytic efficiency of 6Cnts@ZnC.

3.1.3 SEM, TEM &HrTEM. Surface morphology of the Cnts, ZnC, and *x*Cnts@ZnC samples is examined by scanning electron microscope (SEM; S-4800 device HITACHI), as depicted in Fig. 3A–C. The SEM images reveal that Cnts have a uniform and tubular morphology, with diverse lengths and no aggregation.[45] The ZnC sample is made up of hexagon-shaped nanosheets that are evenly distributed and grouped. The precipitation ZnC on Cnts effectively demonstrates the difference in morphology. The transmission electron microscopy (TEM; JOEL JEM 2100) image of the 6Cnts@ZnC sample reveal a strong bond between the ZnC nanosheets and the Cnts tuber resulting in an increased number of active sites for the reactants.[46] This attachment results in a substantial reduction in the length of the tubes and the development of numerous truncated, broken tubes. Furthermore, the mean tube diameter exhibits irregular increments. The above changes provide advantageous circumstances for the segregation and conveyance of electrons and holes in hydrid materials.

Further, the measurement of the distance between the lattice fringes in high resolution mode (HrTEM; JOEL JEM 2100) shows values of 0.28 nm and 0.251 nm, respectively, corresponding to the (100) plane of ZnO[47] and the (311) plane of $ZnCo_2O_4$.[48,49]

3.1.4 XPS. Analyze the chemical composition and bonding characteristics of ZnC and 6Cnts@ZnC samples using the X-ray photoelectron spectroscopy (XPS; ULVAC-PHI) (Fig. 4A). The full XPS spectrum of the ZnC sample consists of the elements zinc (Zn), oxygen (O), and cobalt (Co), while the 6Cnts@ZnC sample includes the elements zinc (Zn), oxygen (O), carbon (C) and cobalt (Co). No additional elements were present in either sample; their composition was precisely established based on the precursor.

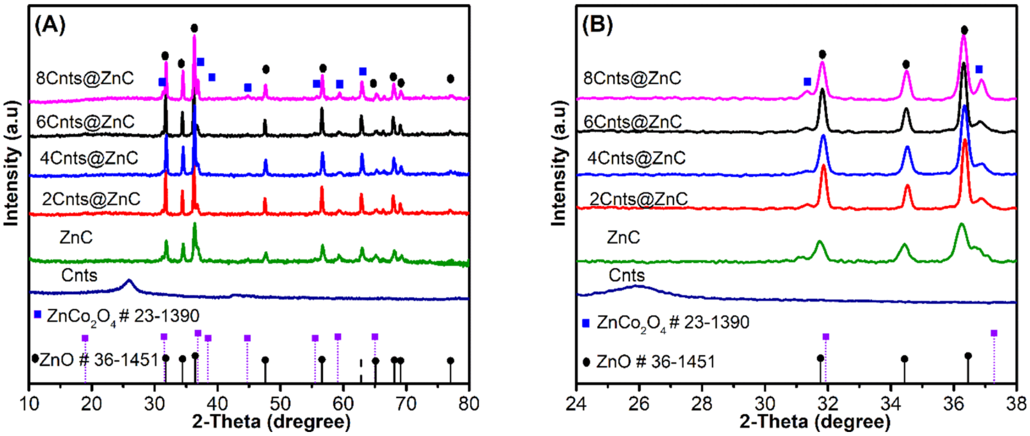

Fig. 1 (A and B) XRD patterns of (a) Cnts, ZnC and *x*Cnt@ZnC ($x = 2, 4, 6, 8$).

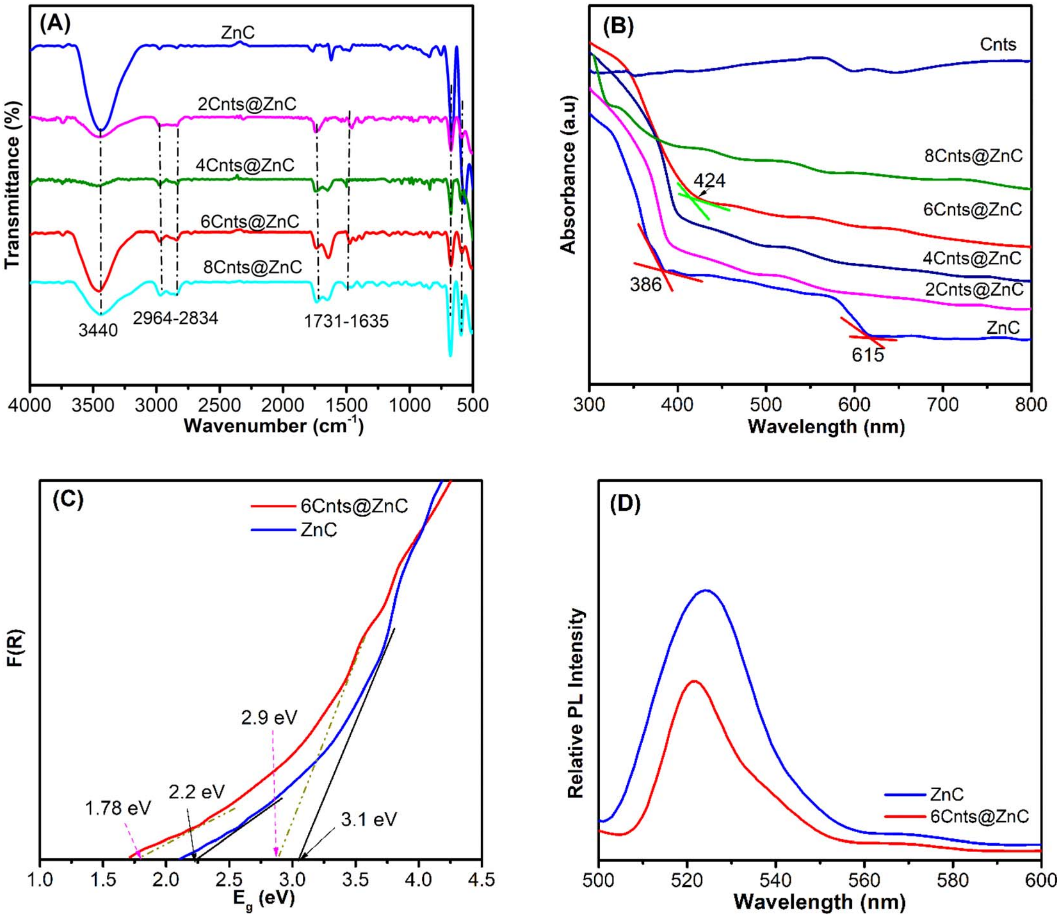

Fig. 2 (A) FT-IR and (B) UV-vis DRS patterns of Cnts; ZnC; *x*Cnt@ZnC ($x = 2, 4, 6, 8$). (C) E_g of ZnC and 6Cnts@ZnC; (D) PL of ZnC and 6Cnts@ZnC.

The deconvolution C 1s of the 6Cnts@ZnC sample in high resolution spectrum has three peaks with energy levels 284.28, 285.75 and 287.98 eV which are the bonds attributed to the graphitized carbon sp^2 C=C, C–C bond, and C=O bond (Fig. 4B).[50,51] The C=O bond power indicates that there is considerable oxidation in the Cnts network when paired with ZnC, and the graphitized carbon sp^2 signal of C 1s indicates that there is an interaction between Cnts and ZnC.[13] In addition, the ZnC and 6Cnts@ZnC samples show an apparent shift in the high-resolution XPS spectra of Zn 2p, indicating the creation of chemical interactions at the interface between Zn and C. The binding energies (B.E.) of the Zn 2p$_{3/2}$ and Zn 2p$_{1/2}$ peaks in pure ZnC are 1020.78 and 1043.88 eV, respectively. However, in the case of 6Cnts@ZnC, the associated peaks exhibit B.E. of 1021.28 and 1044.38 eV, respectively. The observed increase in B.E. at the Zn 2p position of 6Cnts@ZnC, relative to the Zn 2p location of ZnC, suggests that there is an electron transfer from ZnC to Cnts[13] (Fig. 4C). The XPS spectra of Co 2p exhibits two prominent wide peaks, which correspond to Co 2p$_{3/2}$ and Co 2p$_{1/2}$ (Fig. 4D).[52] Furthermore, two minor peaks in this spectrum (B.E. 789, 805 eV) linked to satellite shaking give additional evidence for the presence of multivalent cobalt (Co^{3+} and Co^{2+}).[53] Two peaks with B.E. 779.38 and 780.53 eV are included in the decoding results based on the Gaussian of the peak at value Co 2p$_{3/2}$, and two peaks with B.E. 794.43 and 795.66 eV are included in the decoding results at value Co 2p$_{1/2}$. Previous research on the characteristics of multivalent Co indicates that Co^{3+} is represented by two peaks with B.E. of 779.38 and 794.43 eV, whereas Co^{2+} is represented by two peaks with B.E. of 780.53 and 795.66 eV.[54,55] The B.E. of Co 2p in 6Cnts@ZnC exhibits a clear shift towards higher values compared to the B.E. of Co 2p in ZnC. The high resolution XPS spectra of O 1s region of ZnC at B.E. of 528.72, 529.72 and 531.47 eV, as displayed in Fig. 4E, are indicative of typical metal–oxygen bonds (lattice oxygen – O$_L$) oxygen vacancies – O$_v$, and oxygen absorbed on the surface – Ow.[51,56,57] The XPS spectra of the O 1s region of 6Cnts@ZnC exhibit three distinct peaks, with higher binding energies compared to the O 1s spectrum of ZnC. The study results indicate a slight positive change in the binding energy at O 1s, Zn 2p, and Co 2p of the 6Cnts@ZnC sample in comparison to the ZnC sample. This indicates that the bond state and charge distribution of elements in the 6Cnts@ZnC sample suffered changes, leading to a decrease in electron density at these positions.[18,58] Consequently, there is an increase in bond energy. Energy level changes like this show that Cnts and ZnC interact chemically to produce Zn–C and Co–C bonds in the

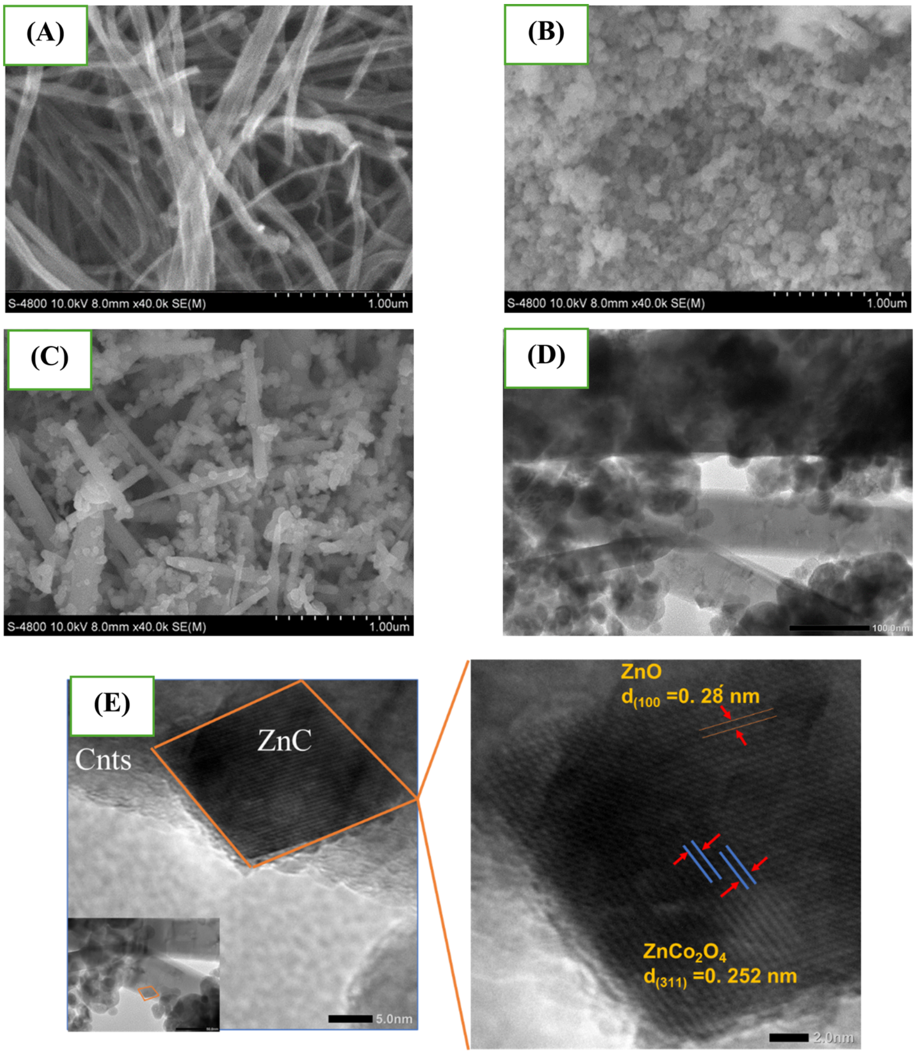

Fig. 3 (A–C) SEM patterns of Cnts; ZnC and 6Cnts@ZnC; (D) TEM & (E) HrTEM of 6Cnts@ZnC.

6Cnts@ZnC material.[51,59] They also facilitate the transfer of 6Cnts@ZnC electrons from ZnC's surface to Cnts.[49,60]

Fig. 5 displays the EDS result for the samples ZnC and Cnts@ZnC. Sample ZnC contains the elements C (2.17 wt%), O (22.87 wt%), Co (15.44% wt%), and Zn (61.69% wt%), whereas sample 6Cnts@ZnC contains the elements C (3.5 wt%), O (22.29 wt%), Co (13.16 wt%), and Zn (61.05 wt%).

3.2 Catalytic activity

3.2.1 Effect of Cnts@ZnC with different mass of Cnts. Fig. 6A illustrates the outcomes of assessing the photocatalytic efficiency of Cnts, ZnC, and *x*Cnts@ZnC treated OFL. The test occurred under particular conditions, including catalyst amount of 1 g L^{-1}, a light off 60 minutes, a light on 240 minutes, initial OFL concentration of 20 ppm, and pH 8. Cnts remove 45% of OFL with strong adsorption capability, but they are nearly incapable of breaking down OFL through photocatalysis. OFL degradation *via* ZnC pure under visible light displays low obvious efficiency (53.3%; $k = 0.0037$ $\min^{-1}$).

In 60 minutes, ZnC and *x*Cnts@ZnC were able to remove 6–10% of the OFL reach desorption equilibrium, but the OFL degradation efficiency changed significantly (62.5–85.8%) during light on. Those experimental findings also show that the OFL decomposition efficiency of *x*Cnts@ZnC ($x = 2, 4, 6$) has been significantly enhanced when increasing the Cnts mass from 20 to 60 mg, with 6Cnts@ZnC demonstrating its highest OFL decomposition efficiency, reaching (85.8%; $k = 0.0099$ $\min^{-1}$). When compared to ZnC, the OFL decomposition rate constant of 6Cnts@ZnC is three times higher. These are 2 reason: (i) Cnts possess a large surface charge. Thus, the precipitation of ZnC onto Cnts will result in an increase of the surface area of the *x*Cnts@ZnC hydrid. This increase in area will enhance the adsorption capacity and boost the photoactivity of the *x*Cnts@ZnC hydrid.[61,62] (ii) Additionally, the Cnts function as pathways for the transport and capture of electrons, which promotes electron mobility on the *x*Cnts@ZnC surface and lengthens the lifetime of photoelectrons. This results in reduced recombination between photogenerated electrons and holes, boosting the photocatalytic activity of *x*Cnts@ZnC.[40,45,63]

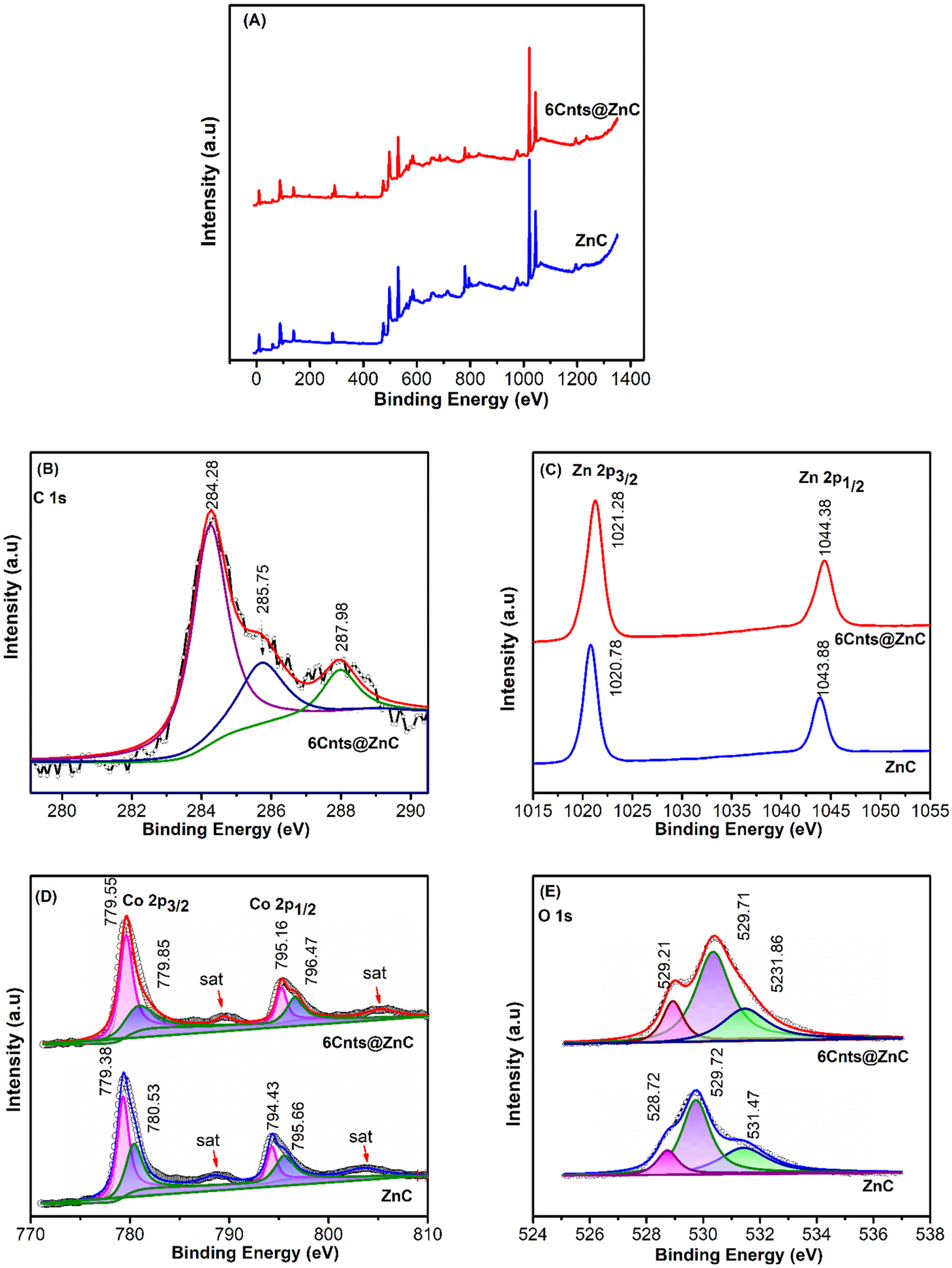

Fig. 4 XPS survey spectra (A); high resolution core level spectra of (B) C 1s; (C) Zn 2p; (D) Co 2p; and (E) O 1s for ZnC and 6Cnts@ZnC.

However, the OFL degradation efficiency of the 8Cnts@ZnC hybrid photocatalyst diminished to 70.7% ($k = 0.0057$ min^{-1}). The explanation could be that when increasing loading Cnts (80 mg) is combined with ZnC, too much black Cnts is deposited on ZnC, which prevents ZnC from absorbing light. These can decrease the efficiency of electron transfer between the Cnts and ZnC, resulting in an increased rate of electron recombination and hole generation by photoexcitation. Therefore, the OFL degradation efficiency of 8Cnts@ZnC decreased.[61,62,64]

After analyzing the catalytic process of composites using the first-order kinetic equation, we obtained R^2 values ranging from 0.9171 to 0.93622 (Fig. 6B). This establishes that the OFL breakdown process of *x*Cnts@ZnC catalysts are accurately described *via* the first-order kinetic equation. The results indicated that the efficiency and degradation rate of OFL in the *x*Cnts@ZnC followed an established order: 6Cnts@ZnC (85.8%; $k = 0.0099$ min^{-1}) > 4Cnts@ZnC (79.5%; $k = 0.0078$ min^{-1}) > 8Cnts@ZnC(70.7%; $k = 0.0057$ min^{-1}) > 2Cnts@ZnC (62.5%; $k = 0.0049$ min^{-1}) > ZnC (53.3%; $k = 0.0037$ min^{-1}). Therefore,

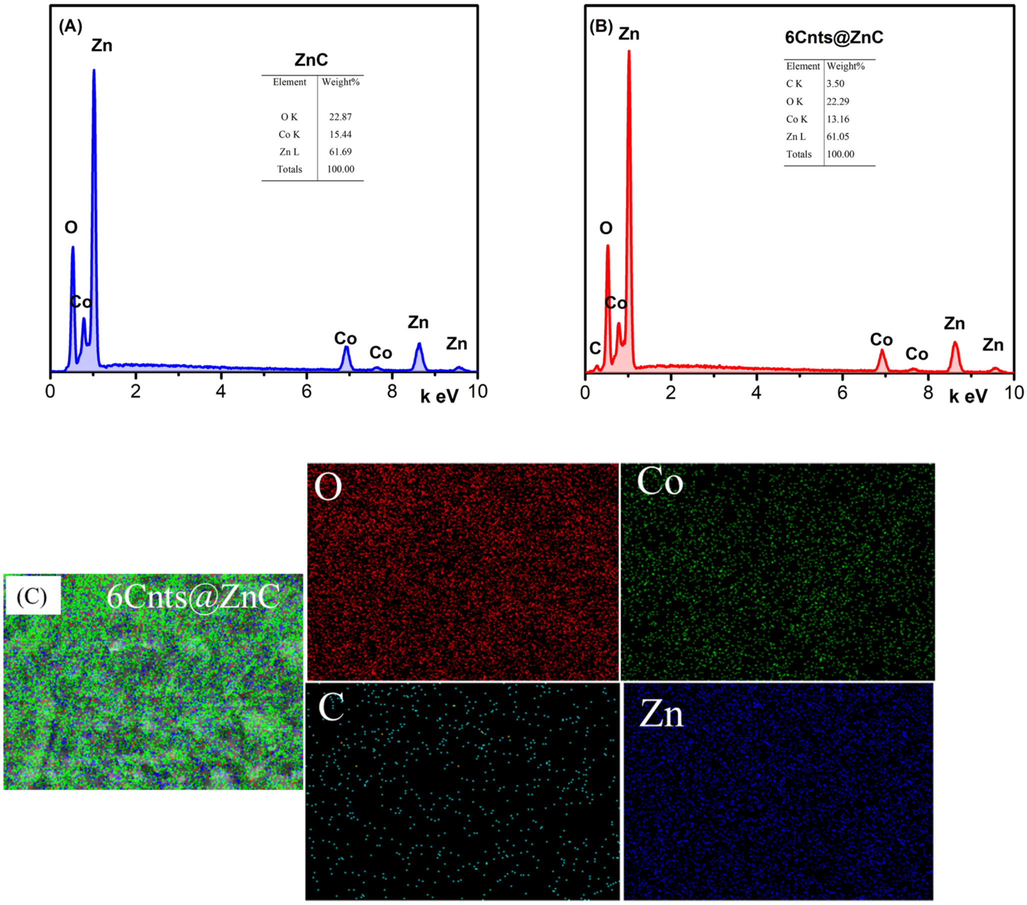

Fig. 5 (A and B) EDS image of ZnC and 6Cnts@ZnC; (C) EDS elemental mapping images of 6Cnts@ZnC.

the 6Cnts@ZnC hybrid was selected as the optimal to continue photocatalytic optimization.

3.2.2 Effect of the amount of 6Cnts@ZnC hybrid. The impact of the loading of 6Cnts@ZnC on its capacity to break down OFL in the visible light range was investigated *via* varying the loading of 6Cnts@ZnC from 0.2 to 2 g L^{-1}. The results presented in Fig. 6C show while the mass of 6Cnts@ZnC increased from 0.2 to 2 g L^{-1}, the efficiency of OFL decomposition increased from 30.2% to 85.8% (k = 0.0017–0.0099 min^{-1}). Nevertheless, when the mass of 6Cnts@ZnC rose to 2 g L^{-1}, the frequency of OFL decomposition dropped to 70.6% (k = 0.0056 min^{-1}). According to research on the relationship between the loading of catalyst and photodegradation efficiency, this result shows that when the loading of catalyst increases, degradation efficiency increases to a point max and then decreases. Nevertheless, if the loading of catalyst is added in excess, the solution gets cloudy and forms a suspension that prevents light from passing through it, which lowers photocatalytic efficiency.[40,65,66] Besides, significant loading of catalyst may also cause the particles to clump together, decreasing the surface area in contact with the solution and lowering photocatalytic efficiency.[40]

3.2.3 Effect of initial concentration. The concentration of the pollutant has a significant impact on photocatalytic efficiency.[65,67] This investigation examined OFL concentrations ranging from 5 to 30 ppm; loading 6Cnts@ZnC of 1 g L^{-1}, pH 8, adsorption duration of 60 min, and an irradiation time of 240 min (Fig. 6D). Under light irradiation, OFL at concentrations of 5 and 10 ppm fully decomposes after 120 minutes and 240 minutes, respectively. The OFL decomposition efficiency of 6Cnts@ZnC steadily declines as OFL concentration rises. Decomposition efficiency dropped to 85.8% ($k = 0.0099$ min^{-1}) and 62.1% ($k = 0.0049$ min^{-1}) at concentrations of 20 ppm and 30 ppm. The generation of oxidants $^{\bullet}OH$, $O_2^{\bullet-}$ on the 6Cnts@ZnC catalyst surface the catalyst surface remains constant under a steady light source, so these oxidants are insufficient to degrade pollutants at elevated concentrations, resulting in diminished decomposition efficiency.[67,68]

3.2.4 Effect of pH. In this work, we examined the impact of pH on the OFL degrading capacity of 6Cnts@ZnC in a range of pH 4–10 settings. Fig. 7 illustrates the three cationic (OFL^{+}), Zwitterionic ($OFL^{\pm}$), and anionic (OFL^{-}) properties of OFL that are associated with variations in pH values: $pH < pK_{a1}$ (5.9), $pK_{a1} < pH < pK_{a2}$, and $pH > pK_{a2}$ (8.3).[6,69] The isoelectric point (pH_{pzc}) of 6Cnts@ZnC was found to be 7.7. Thus, $pH < pH_{pzc}$, 6Cnts@ZnC have positive charge, whereas $pH > pH_{pzc}$, 6Cnts@ZnC have negative charge.[69]

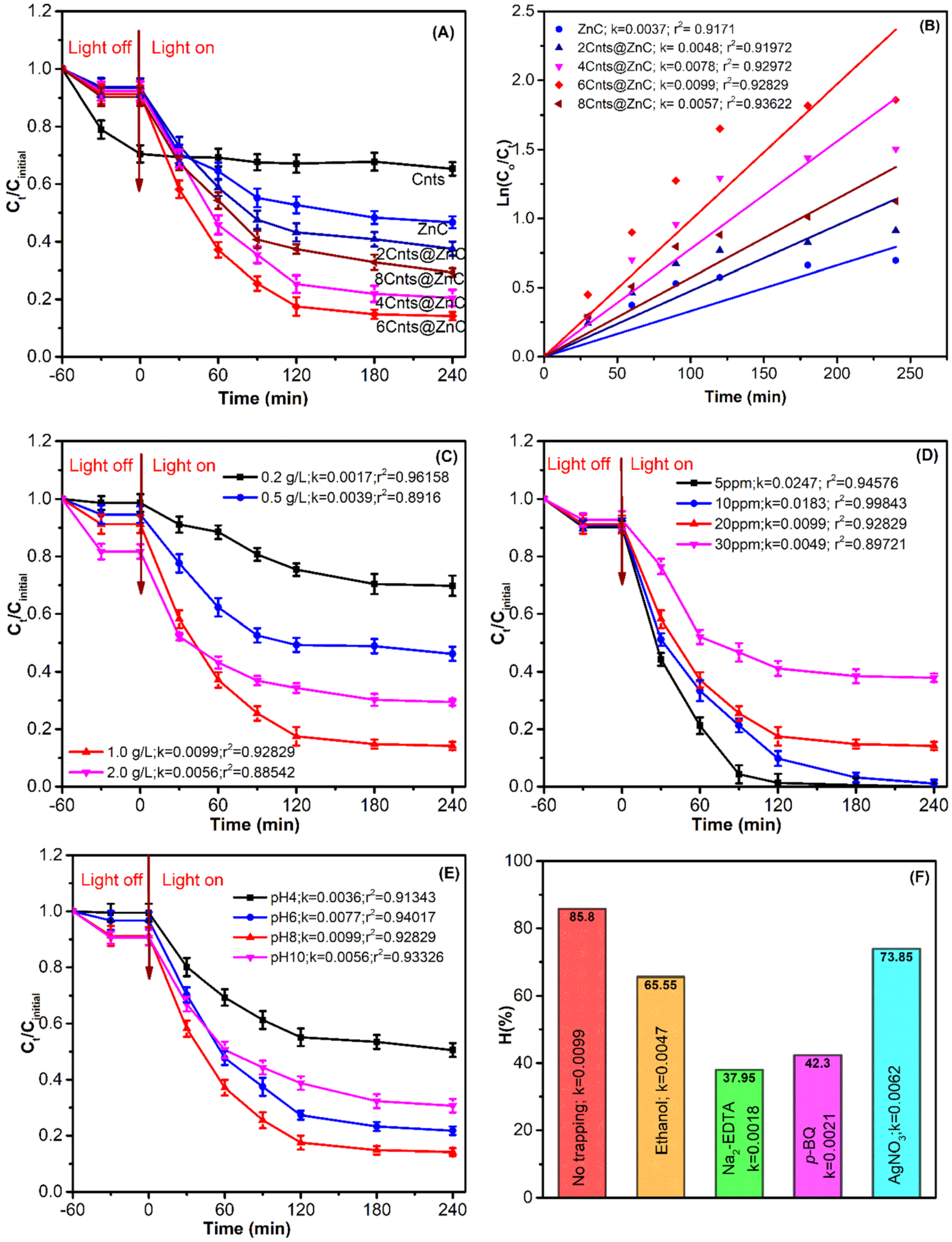

Fig. 6 (A and B) Effect of Cnts@ZnC with different mass of Cnts and ate constants of photocatalysts. (C) Effect of the amount of 6Cnts@ZnC hybrid (amount of 6Cnts@ZnC hybrid: 0.2–2.0 g L^{-1}; initial OFL concentration: 20 ppm; pH 8). (D) Effect of initial concentration (initial OFL concentration: 5–30 ppm; amount of 6Cnts@ZnC hybrid: 1.0 g L^{-1}; pH 8). (E) Effect of pH (pH 4–10; amount of 6Cnts@ZnC hybrid: 1.0 g L^{-1}; initial OFL concentration: 20 ppm; pH 8). (F) Trapping experiments (the "trapping" of free radicals $^{\bullet}$OH, $O_2^{\bullet -}$, h$^+$, and e$^-$ using ethanol, *p*-BQ, Na$_2$-EDTA, and AgNO$_3$).

According to experimental findings, OFL breakdown has a low photocatalytic effectiveness at pH 4 (49.4%; k = 0.0036 min^{-1}). At this stage (pH 4 < pK_{a1}), the positive charge 6Cnts@ZnC and OFL$^+$ face electrostatic repulsion. At pH 6 and pH 8 (pK_{a1} < pH < pK_{a2}), OFL happens in a zwitterionic state, meaning it carries both positive and negative charges on the same molecule (OFL$^{\pm}$). As a result, the adsorption capacity of OFL on 6Cnts@ZnC is increased, leading to an enhanced photocatalytic efficiency. The results showed that the photocatalytic efficiency of the OFL degradation of 6Cnts@ZnC highest at pH 8. Previous research indicates that $^{\bullet}$OH is the primary oxidant in an alkaline environment.[69] Results of the experiments also indicate that $^{\bullet}$OH also a factor in the OFL breakdown of Cnts@ZnC. During this period (pH 8), the concentration of OH$^-$ grows and it reacts with photogenerated holes as shown in eqn (1) and (2), which raises the amount of $^{\bullet}$OH according to reaction 2 of antibiotic degradation.[8]

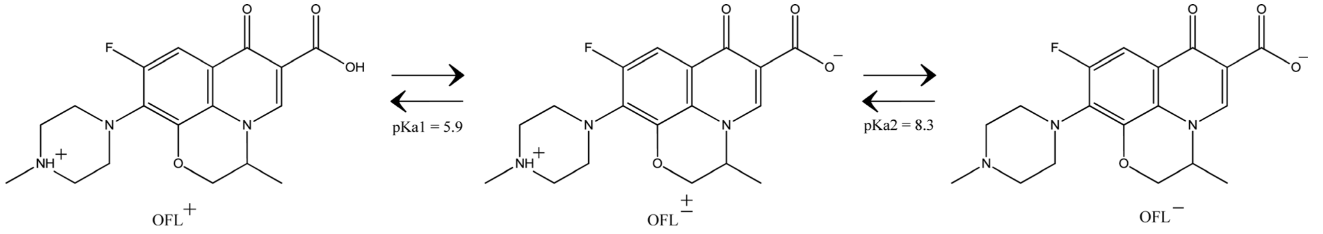

Fig. 7 The three cationic (OFL^+), Zwitterionic ($OFL^{\pm}$), and anionic (OFL^-) properties of OFL.[5,70]

At pH 10 > pK_{a2}, the carboxy group on the quinolone ring undergoes deprotonation, resulting in the conversion of the OFL molecule from its neutral state to a negatively charged OFL^- state. This leads to a repulsive interaction between OFL^- and 6Cnt@ZnC, which is also negatively charged. Furthermore, a high level of OH^- may react with both $^\bullet OH$ radicals and photogenerated holes (as seen in eqn (3) and (4)),[71] so slowing the decomposition of OFL and leading to a decrease in photocatalytic efficiency at pH 10 (69.35%; $k = 0.0056\ min^{-1}$).

$$h^+ + OH^- \rightarrow {}^\bullet OH \tag{1}$$

$$^\bullet OH + OFL \rightarrow OFL^* \rightarrow \text{degradation products} \tag{2}$$

$$^\bullet OH + OH^- \rightarrow H_2O + O^\bullet \tag{3}$$

$$4h^+ + 4OH^- \rightarrow O_2 + 2H_2O \tag{4}$$

3.2.5 Trapping experiments & photocatalytic mechanism.

Advanced oxidation processes (AOPs) involve the decomposition of organic material *via* oxidants such as $^\bullet OH$, $O_2^{\bullet -}$, h^+ and e^-.[1] So, it is imperative to determine the primary factors involved in the decomposition of organic substances. The ethanol, *p*-benzoquinone (*p*-BQ), Na_2-EDTA and $AgNO_3$ were added to the photocatalytic system in that order after we started the light irradiation to "traping" $^\bullet OH$, $O_2^{\bullet -}$, h^+ and e^-.[72] The research findings in Fig. 6F show that the photocatalytic efficiency of the system drops to 37.95% ($k = 0.0018\ min^{-1}$) and 42.3% ($k = 0.0021\ min^{-1}$) when Na_2-EDTA and *p*-BQ are added, while a photocatalytic efficiency of 85.8% ($k = 0.0099\ min^{-1}$) occurs when no trapping is used. In contrast, the addition of $AgNO_3$ and ethanol resulted in a drop in photocatalytic efficiency to 73.85% ($k = 0.0062\ min^{-1}$) and 65.55% ($k = 0.0047\ min^{-1}$). This discovery suggests that h^+ and $O_2^{\bullet -}$ play a major role in the breakdown of OFL by 6Cnts@ZnC, while $^\bullet OH$ and and e^- have a minimal impact.

Use the Taus formula,[41] $(\alpha h\nu)^2 = A(h\nu - E_g)$, to determine the energy of the band gap of the synthesized material. Fig. 2C shows that the band gap energy of ZnC is 3.1 V for ZnO and 2.2 eV for $ZnCo_2O_4$. The band gap energy of 6Cnst@ZnC are 2.9 and 1.78 eV, respectively. Formula calculates the potential of the conduction and valence domains.[38,39]

$$E_{vb} = X - E_e + 0.5\ E_g \tag{5}$$

$$E_{cb} = E_{vb} - E_g \tag{6}$$

where X is the absolute electronegativity of semiconductor materials, E_e is the free electron energy on the hydrogen electrode scale (4.50 eV). The conduction band energy (E_{cb}) and valence band energy (E_{vb}) values for ZnC and 6Cnts@ZnC samples were determined in Table S.1.†

The 6Cnts@ZnC hybrid is exposed to visible light, $ZnCo_2O_4$ ($E_g = 1.78$ eV) is excited, generating a significant amount of photogenerated electrons and h^+ pairs, whereas ZnO ($E_g = 2.9$ eV) can only absorb a fraction of the visible light, resulting in several fewer photogenerated electrons and h^+ pairs. The E_{cb} of ZnO ($E_{cb} = -0.16$ eV) is higher than the reduction potential of $O_2/O_2^{\bullet -}$ (−0.33 eV *vs.* NHE), therefore, the photogenerated electrons on the CB of ZnO are unable to transform O_2 to $O_2^{\bullet -}$. On the contrary, the $ZnCo_2O_4$ phase has a more negative E_{cb} ($E_{cb} = -0.45$ eV) the reduction potential of $O_2/O_2^{\bullet -}$. As a result, the photo generated electrons on the CB of the $ZnCo_2O_4$ phase can reduce O_2 to $O_2^{\bullet -}$. Additionally, these photo generated electrons can also transfer to the CB of ZnO and combine with the electrons on the CB of the ZnO phase, which then move directly to the Cnts. The large Cnts network functions as a highly effective electron trap, gathering photoexcited electrons from the CB of transported ZnO, so inhibiting the recombination of electron–hole pairs. Afterwards, electrons move towards the surface and react with the adsorbed O_2 on *x*Cnts@ZnC, leading to the creation of $O_2^{\bullet -}$ radicals. These radicals have the capability to break down OFL, resulting in the production of degradation products. Alternatively, these electrons that have been stimulated by light can directly interact with OFL, leading to the creation of degradation products.

The typical oxidation potential of $H_2O/^\bullet OH$ (+2.40 eV *vs.* NHE) is less than the E_{vb} of ZnO ($E_{vb} = +2.74$ eV) so the photogenerated h^+ holes of $ZnCo_2O_4$ can oxidize H_2O adsorbed produces a significant amount of $^\bullet OH$ radicals, these $^\bullet OH$ radicals decompose OFL to create degradation products. In addition, the h^+ of $ZnCo_2O_4$ can directly decompose OFL to create degradation products. Furthermore, because of the differing E_{vb} of ZnO and $ZnCo_2O_4$, a portion of the h^+ in ZnO's VB migrates to $ZnCo_2O_4$'s VB and combines with its h^+ to directly break down OFL and produce the degradation products. The E_{vb} of $ZnCo_2O_4$ ($E_{vb} = +1.33$ eV) is less than the typical oxidation potential of $H_2O/^\bullet OH$, hence the h^+ photo-generated hole of $ZnCo_2O_4$ is unable to oxidize H_2O to make $^\bullet OH$. Based on the results mentioned previously, eqn (7)–(14) and Fig. 8 can be used to predict the OFL decomposing process of *x*Cnts@ZnC.

$$\text{Cnts@ZnC} + h\nu \rightarrow \text{ZnC}\ (e^-) + \text{ZnC}\ (h^+) + \text{Cnts} \quad (7)$$

$$\text{ZnC}\ (e^-) + O_2 \rightarrow O_2^{\bullet -} \quad (8)$$

$$\text{ZnC}\ (e^-) + \text{Cnts} \rightarrow \text{Cnts}\ (e^-) \quad (9)$$

$$\text{Cnts}\ (e^-) + O_2 \rightarrow O_2^{\bullet -} \quad (10)$$

$$O_2^{\bullet -} + \text{OFL} \rightarrow \text{degradation products} \quad (11)$$

$$h^+\ (\text{ZnC}) + H_2O \rightarrow H^+ + {}^{\bullet}OH \quad (12)$$

$$^{\bullet}OH + \text{OFL} \rightarrow \text{degradation products} \quad (13)$$

$$h^+\ (\text{ZnC}) + \text{OFL} \rightarrow \text{degradation products} \quad (14)$$

3.2.6 The degradative pathway and potential toxicity assessment. The environmental impact of the byproduct generated from the degradation of organic matter by photocatalysts is significant. Through the utilization of HPLC-MS analysis, we can accurately determine the intermediate compound involved in the breakdown process of the 6Cnts@ZnC photocatalyst's OFL. The Liquid chromatography column: a linear ion trap LCMS system from Thermo, USA, with an equilibrium liquid chromatography column (LC-MS) and a flow rate of 0.3 mL min^{-1}, was used to perform OFL degregation on a 5 μL injection volume containing a 20 ppm concentration of methanol solvent, followed by ionisation and ESI (+). No column was used. Here are the optimal operating conditions for full-scan mass spectrometry: 4.0 kV for the probe, 350 °C for the heat source, 250 °C for the capillary, 30 mL min^{-1} for the sheath gas, and 10 mL min^{-1} for the auxiliary gas. The HPLC-MS analysis is conducted using ESI with positive ionization, namely $[M + H]^+$. Fig. 9 shows the defragmentation of OFL at an initial concentration of 20 ppm at different decomposition time intervals: (A) $t = 0$ minutes, (B) $t = 60$ minutes, (C) $t = 120$ minutes, (D) $t = 180$ min, (E) $t = 240$ minutes, and (F) $t = 300$ minutes. Fig. 9A shows that at $t = 0$ min, the primary fragment is the mother ion molecule with a mass-to-charge ratio of $[M + H]^+ = 362.27$, which remains intact without any degradation. This fragment has an intensity of 100%. Fig. 9B shows that at a duration of 60 min, with an average retention time of 0.12, the major fragment ion $[M + H]^+$ had a mass of 274.39. The compound OFL decomposed 93.21% of the initial amount, leaving behind 6.79% as shown in Fig. 10. Fig. 9C shows that the decomposition of OFL was seen after 120 minutes of the catalytic reaction. The decomposition percentage was found to be 94.71%, which equates to 5.29% of the original concentration of OFL, as shown in Fig. 10. During a 120 minutes interval, two additional peaks emerged: one at 304.42 (100% abundance, stable fragment) and another at 332.40 (30% abundance), both in the $[M + H]^+$ ion form. Fig. 9D shows that the composition of OFL after 180 minutes is decomposed with a residue of 4.71%, indicating a decomposition rate of 95.29%. Currently, there are newly identified peaks, including $[M + H]^+$ at 343.34 (30%) and 365.29 (40%). At a duration of 240 minutes, as depicted in Fig. 9E, the degradation rate of OFL was measured to be 95.68%, leaving behind 4.32% of the initial concentration. Additionally,

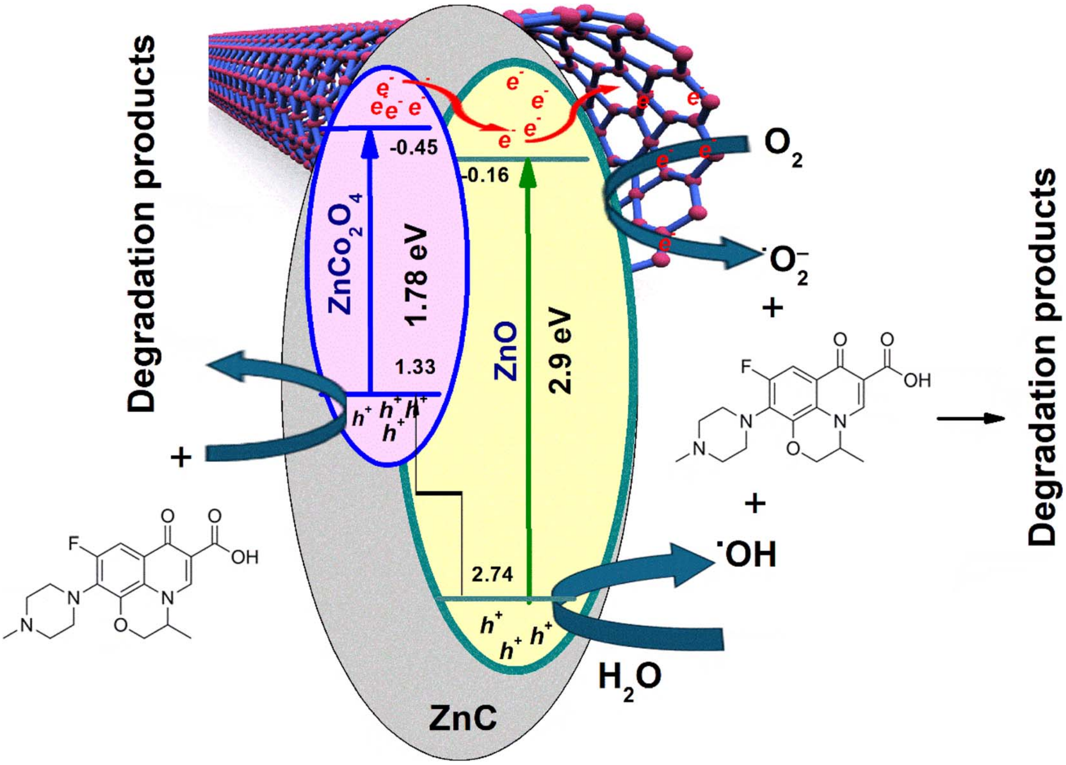

Fig. 8 Proposed photocatalytic mechanism responsible for the degradation of OFL by *x*Cnts@ZnC hydrid.

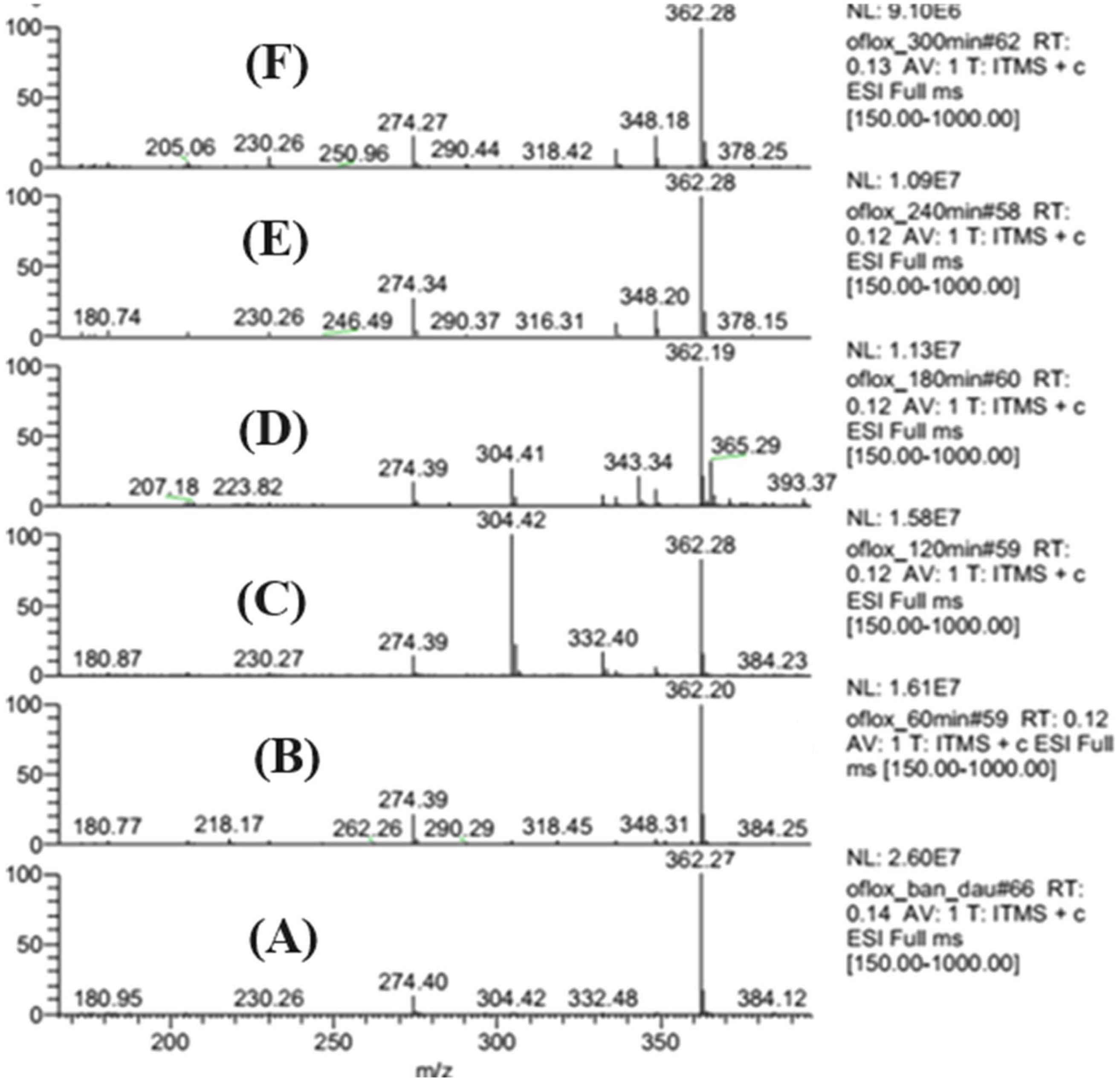

Fig. 9 The degradation of OFL at initial concentration of 20 ppm in different times of 6Cnts@ZnC hybrid: (A) $t = 0$ min; (B) $t = 60$ min; (C) $t = 120$ min; (D) $t = 180$ min; (E) $t = 240$; and (F) $t = 300$ min.

at this specific period, a fragment with a $[M + H]^+$ value of 348.20 emerged. After a duration of 300 minutes, the OFL had undergone decomposition to a degree of 96.44% (Fig. 9F).

The fragmentation patterns of ion mother are depicted in Fig. 11. As shown in Fig. 11, OFL exhibits fragmentation into six stable structures, namely (**2**), (**4**), (**6**), route (b) as well as (**3**), (**5**), and (**7**), route (a) by two pathways. Compound (**2**) is synthesized from (**1**) through oxidative cleavage *via* a free radical reaction involving a damaged methylene group, as depicted in Fig. 11 along pathway (a). The structure (**4**) was formed through oxidative cleavage *via* free radical events and decarboxylation reactions. The chemical (**6**) was synthesized through oxidative cleavage *via* a free radical reaction, resulting in the removal of one C═O double bond and the reduction of one hydrogen molecule. The pathway (b) involves the elimination of a methylene group through oxidative cleavage *via* a free radical reaction, forming compound (**3**). Compound (**5**) is formed through oxidative clearing by means of a free radical reaction and subsequent decarboxylation. Compound (**7**) was synthesized through oxidative cleavage using a free radical reaction, resulting in the removal of one C═O double bond and the reduction of one hydrogen molecule. The process of OFL degradation has been illustrated in Fig. 11, which is a ground-breaking proposition by us based on experimental evidence.

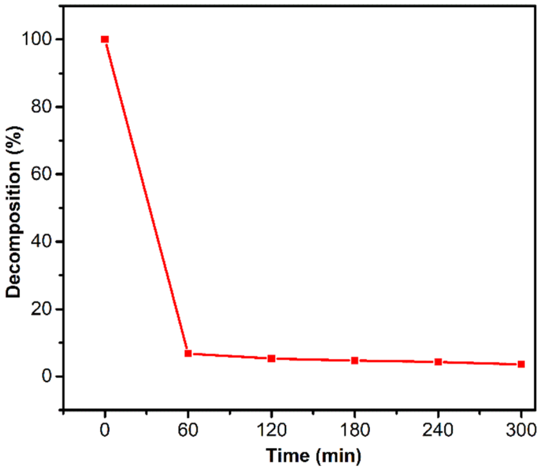

Fig. 10 The decomposition of OFL at different times at initial concentration of 20 ppm.

The OFL exhibits a high degree of decomposability when subjected to a catalytic reaction for 300 min at an initial concentration of 20 ppm. Many previous titles about degradation of OFL has been conducted[73–78] and our work conducted giving smaller molecule in degradation path as seen in Fig. 10, such as (**6**) or (**7**). Compound (**6**) or (**7**) is a pair of isomers that molecules are 273.31. The molecule (**7**) or (**6**) is formed by oxidative cleavage *via* free radical reaction that is removed one methylene group from methyl groups attached to two hetero cyclic rings of mother molecule, OFL. The transform path of OFL has some similarity structures with article at intermedia fragment ion molecule of 347.13 or compound (**2**) or (**3**) and 303.33 or molecule (**4**)/(**5**) as seen in Fig. 9 in this article and Fig. 11 at reference article *via* intermedia compounds.[74]

The predictions of compounds after completing of degradation such as physiochemistry, medicinal chemistry, metabolism, excretion, toxicity, and environmental toxicity parameters that used ADMET model in medicinal chemistry of pure compound like drug such as light compound (**6**) in Fig. 11.[24–26,79] Calculation results from ADMET model of compound (**6**) are indicated in Tables S.2–S.7† that reduced some tables the less relative to process the environment as this project target such as absorption, distribution, metabolism, and toxic pathway properties because they belong to medicinal pharmacy properties. As indicated in Table S.2,† the physicochemical properties of compound (**6**) are in ranges. Compound (**6**) exposed less solubility in water by $\log P = 2.704 > 0$ and $\log S = -3.669 < 0$. The medical chemistry of (**6**) are in full permission ranges and some significant parameters are Lipinski rule, Pfizer Rule, Golden Triangle are in permission domains, and it proved compound (**6**) has properties like drugless as seen Table S.3.† There are no alerts from medicinal chemistry parameters. As seen in Table S.4,† the properties of the drug metabolism of compound (**6**) indicated by enzyme inhibitors or substrate that these CYPs responsible for phase I reactions are concentrated in the liver. The metabolism parameters are CYPs in ranges that proved this compound has no effects on the liver. The excretion properties of (**6**) are exposed in Table S.5† and proved that compound (**6**) has short half-life because of the low value of $T_{1/2}$. The clearance

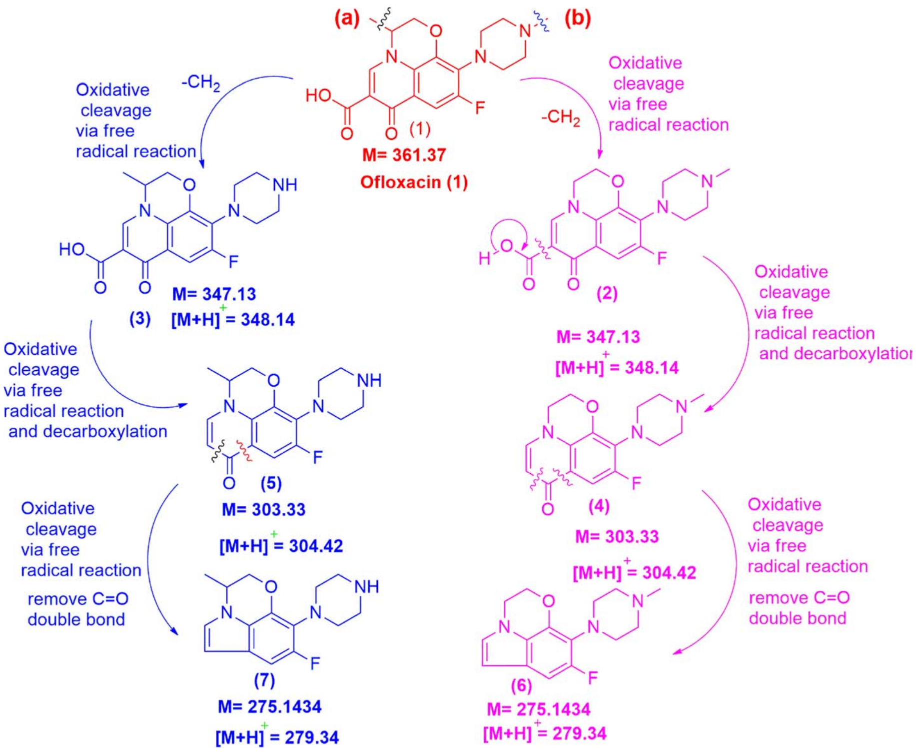

Fig. 11 The decomposition mechanis of OFL *via* oxidative cleavage *via* free radical reaction.

is a significant pharmacokinetic parameter that defines, together with the volume of distribution, the half-life, and thus the frequency of dosing of a drug. The CL of 6.709 is moderate dosing. The toxicity of compound (**6**) is indicated in Table S.6,† as seen in Table S.6,† a few parameters of compound (**6**) have toxicity in human body such as hepatotoxicity *via* H-HT value of 0.899 and drug induced lever injury by DILI value of 0.942. As exposed in Table S.7,† the properties of environmental toxicity of compound (**6**) are indicated that it has nontoxic in environmental site because parameters are optimal ranges. The ADMET model has proved that compound (**6**) is intermedia defragment that has without toxic to environment.

4 Conclusions

Using co-precipitation and thermal methods, we were able to successfully synthesis the *x*Cnt@ZnC hydrid. The *x*Cnts@ZnC hydrid exhibits photocatalytic activity for OFL breakdown. The results indicated that 6Cnts@ZnC demonstrated the greatest efficacy in degrading 85.8% of OFL under visible light. The optimal parameters for this process were a catalyst mass of 1 g L^{-1}, an OFL concentration of 20 ppm, an adsorption time of 60 minutes, visible light irradiation of 240 minutes, and pH 8. The combination of Cnts and ZnC creates the avorable conditions for efficient segregation of electrons and holes. Through their ability to capture electrons produced by conductivity, Cnts serve to prevent photogenerated electrons and holes recombination. Plus, the catalytic mechanism and intermediate stages of the OFL breakdown of *x*Cnts@ZnC were predicted. The *x*Cnts@ZnC hybrid breaks down the OFL solution in the visible lighting region, according to the first-level kinetic equation. It was demonstrated using the ADMET model that the small molecules produced by the OFL breakdown of the *x*Cnts@ZnC hybrid are not environmentally hazardous. Because of its high stability, facile synthesis, and great endurance, we anticipate that *x*Cnts@ZnC will aid in the development of photocatalytic materials in the treatment of pollution.

Data availability

The data supporting this article has been included as part of the ESI.†

Conflicts of interest

The authors declare that they have no known competing interests that could have appeared to influence the work reported in this paper.

References

1 B. Tan, Y. Fang, Q. Chen, X. Ao and Y. Cao, *Opt. Mater.*, 2020, 110470, DOI: 10.1016/j.optmat.2020.110470.
2 P. Barathe, K. Kaur, S. Reddy, V. Shriram and V. Kumar, *J. Hazard. Mater. Lett.*, 2024, 100105, DOI: 10.1016/j.hazl.2024.100105.
3 R. Haghniaz, A. Rabbani, F. Vajhadin, T. Khan, R. Kousar, A. R. Khan, H. Montazerian, J. Iqbal, A. Libanori, H. J. Kim and F. Wahid, *J. Nanobiotechnol.*, 2021, 1–15, DOI: 10.1186/s12951-021-00776-w.
4 H. Peng, B. Pan, M. Wu, R. Liu, D. Zhang, D. Wu and B. Xing, *J. Hazard. Mater.*, 2012, **211–212**, 342–348.
5 T. Paul, M. L. MacHesky and T. J. Strathmann, *Environ. Sci. Technol.*, 2012, **46**, 11896–11904.
6 G. Zhao, J. Ding, F. Zhou, X. Chen, L. Wei, Q. Gao, K. Wang and Q. Zhao, *Chem. Eng. J.*, 2021, 126704, DOI: 10.1016/j.cej.2020.126704.
7 N. H. Tran, H. Chen, M. Reinhard, F. Mao and K. Y. H. Gin, *Water Res.*, 2016, **104**, 461–472.
8 Q. Wang, P. Li, Z. Zhang, C. Jiang, K. Zuojiao, J. Liu and Y. Wang, *J. Photochem. Photobiol., A*, 2019, **378**, 114–124.
9 T. Zeng, S. Jin, Z. Jin, S. Li, R. Zou, X. Zhang, S. Song and M. Liu, *RSC Adv.*, 2023, **13**, 14048–14059.
10 M. Cheng, G. Zeng, D. Huang, C. Lai, P. Xu, C. Zhang and Y. Liu, *Chem. Eng. J.*, 2016, **284**, 582–598.
11 P. Karthikeyan and S. Meenakshi, *J. Mol. Liq.*, 2019, 111766, DOI: 10.1016/j.molliq.2019.111766.
12 C. Jiehu, W. Chunlei, Z. Ming, Z. Jie, F. Li, D. Xiuhong, C. Leiming and L. Chunguang, *Appl. Surf. Sci.*, 2020, 147564, DOI: 10.1016/j.apsusc.2020.147564.
13 Y. Zhu, P. Wu, S. Yang, Y. Lu, W. Li, N. Zhu, Z. Dang and Z. Huang, *RSC Adv.*, 2016, **6**, 37689–37700.
14 D. Peng, Q. Jing, Z. Feng, J. Niu, X. Cheng, X. Wu, X. Zheng and X. Yuan, *J. Phys. Chem. Solids*, 2020, 109199, DOI: 10.1016/j.jpcs.2019.109199.
15 C. Wang, Z. Wang, J. Xu and Y. Nie, *ACS Omega*, 2021, **6**, 22126–22136.
16 L. Guo, Y. Wu, P. Duan and Z. Zhang, *Constr. Build. Mater.*, 2020, 117256, DOI: 10.1016/j.conbuildmat.2019.117256.
17 L. Zhang, J. Liu, H. Xiao, D. Liu, Y. Qin, H. Wu, H. Li, N. Du and W. Hou, *Chem. Eng. J.*, 2014, **250**, 1–5.
18 J. Jia, D. Li, J. Wan and X. Yu, *J. Ind. Eng. Chem.*, 2016, **33**, 162–169.
19 A. K. Rai, T. V. Thi, B. J. Paul and J. Kim, *Electrochim. Acta*, 2014, **146**, 577–584.
20 G. Zhao, C. Li, X. Wu, J. Yu, X. Jiang, W. Hu and F. Jiao, *Appl. Surf. Sci.*, 2018, **434**, 251–259.
21 A. Shokrgozar, K. Seifpanahi-Shabani, B. Mahmoodi, N. M. Mahmoodi, F. Khorasheh and M. Baghalha, *Desalin. Water Treat.*, 2021, **216**, 389–400.
22 W. Zhang, C. Xu, E. Liu, J. Fan and X. Hu, *Appl. Surf. Sci.*, 2020, 146039, DOI: 10.1016/j.apsusc.2020.146039.
23 N. T. M. Tho, D. N. N. Khanh, N. Q. Thang, Y. I. Lee and N. T. K. Phuong, *Environ. Sci. Pollut. Res.*, 2020, **27**, 11127–11137.
24 G. Xiong, Z. Wu, J. Yi, L. Fu, Z. Yang, C. Hsieh, M. Yin, X. Zeng, C. Wu, A. Lu, X. Chen, T. Hou and D. Cao, *Nucleic Acids Res.*, 2021, **49**, W5–W14.
25 M. Bitew, T. B. Tegene Demissie, A. Belayneh, M. Endale and R. Eswaramoorthy, *PLoS One*, 2021, **16**, e0260853.
26 Y. Wang, J. Xing, Y. Xu, N. Zhou, J. Peng, Z. Xiong, X. Liu, X. Luo, C. Luo, K. Chen, M. Zheng and H. Jiang, *Q. Rev. Biophys.*, 2015, **48**, 488–515.

27 G. Van Vo, T.-H.-T. Nguyen, T.-P. Nguyen, T.-H.-T. Do, N.-M.-A. Tran, T.-H. Nguyen and T. Trang Nguyen, *Saudi Pharm. J.*, 2022, 1301–1314, DOI: **10.1016/j.jsps.2022.06.018**.

28 K. K. H. Ngo, T. K. C. Huynh, T. A. Nguyen, N. B. H. Pham, T. H. A. Nguyen, T. C. T. Nguyen, H. P. Nguyen, N. K. N. Phan, T. H. N. Nguyen, D. Ngoc-Phuong Ho, L. K. Huynh, T. Nguyen Minh An and T. K. D. Hoang, *Results Chem.*, 2024, 101501, DOI: **10.1016/j.rechem.2024.101501**.

29 K. M. Parida and L. Mohapatra, *Chem. Eng. J.*, 2012, **179**, 131–139.

30 J. Wang, B. Wang, Z. Wang, L. Chen, C. Gao, B. Xu, Z. Jia and G. Wu, *J. Colloid Interface Sci.*, 2021, **586**, 479–490.

31 X. Wang, P. Wu, Z. Zhao, L. Sun, Q. Deng, Z. Yin and X. Chen, *J. Mater. Sci.: Mater. Electron.*, 2020, **31**, 4895–4904.

32 N. Sharma, Z. Pap, S. Garg and K. Hernádi, *Appl. Surf. Sci.*, 2019, 143536, DOI: **10.1016/j.apsusc.2019.143536**.

33 N. Sharma, B. Veres, P. Dhiman, Z. Pap, K. Baán, S. Garg and K. Hernadi, *RSC Adv.*, 2021, **11**, 37426–37435.

34 W. Ma, N. Wang, L. Yang, Y. Lu, S. Li, Y. Hou, K. Cao and Y. Yan, *J. Mater. Sci.: Mater. Electron.*, 2019, **30**, 20432–20442.

35 Y. Zhou, S. Feng, C. Ma, W. Wu, Z. Ye, X. Dai, Y. Wang and X. Cao, *Ceram. Int.*, 2022, 31334–31343, DOI: **10.1016/j.ceramint.2022.06.315**.

36 H. Y. Phin, Y. T. Ong and J. C. Sin, *J. Environ. Chem. Eng.*, 2020, 103222, DOI: **10.1016/j.jece.2019.103222**.

37 B. R. C. de Menezes, F. V. Ferreira, B. C. Silva, E. A. N. Simonetti, T. M. Bastos, L. S. Cividanes and G. P. Thim, *J. Mater. Sci.*, 2018, **53**, 14311–14327.

38 N. T. M. Tho, B. T. Huy, D. N. N. Khanh, H. N. N. Ha, V. Q. Huy, N. T. T. Vy, D. M. Huy, D. P. Dat and N. T. K. Phuong, *Korean J. Chem. Eng.*, 2018, **35**, 2442–2451.

39 H. Zhang, Y. Gao, S. Meng, Z. Wang, P. Wang, Z. Wang, C. Qiu, S. Chen, B. Weng and Y. M. Zheng, *Advanced Science*, 2024, 2400099, DOI: **10.1002/advs.202400099**.

40 I. Ahmad, M. S. Akhtar, E. Ahmed and M. Ahmad, *Sep. Purif. Technol.*, 2020, 116892, DOI: **10.1016/j.seppur.2020.116892**.

41 A. C. Swathi and M. Chandran, *J. Appl. Phys.*, 2023, **133**(20), DOI: **10.1063/5.0145796**.

42 F. Liu, S. Dong, Z. Zhang, X. Li, X. Dai, Y. Xin, X. Wang, K. Liu, Z. Yuan and Z. Zheng, *RSC Adv.*, 2019, **9**, 25750–25761.

43 L. K. Babu, H. S. Rao, P. N. R. Kishore, N. L. Reddy, M. V. Sankar and Y. V. R. Reddy, *J. Mater. Res.*, 2023, **38**, 3301–3315, DOI: **10.1557/s43578-023-01054-1**.

44 S. Majumder, N. D. Quang, N. M. Hung, N. D. Chinh, C. Kim and D. Kim, *J. Colloid Interface Sci.*, 2021, **599**, 453–466.

45 W. Liu, J. Zhou and J. Zhou, *J. Mater. Sci.*, 2019, **54**, 3294–3308.

46 S. M. Lam, J. C. Sin, A. Z. Abdullah and A. R. Mohamed, *Fullerenes, Nanotubes Carbon Nanostruct.*, 2014, **22**, 471–509.

47 A. Habibi-Yangjeh, M. Pirhashemi and S. Ghosh, *J. Alloys Compd.*, 2020, 154229, DOI: **10.1016/j.jallcom.2020.154229**.

48 S. Hemamalini and R. Manimekalai, *Bull. Mater. Sci.*, 2024, 7961–7977, DOI: **10.1007/s12034-021-02453-yS**.

49 K. Yang, Y. Zhang, C. Meng, F. F. Cao, X. Chen, X. Fu, W. Dai and C. Yu, *Appl. Surf. Sci.*, 2017, **391**, 635–644.

50 Y. Wang, X. Zhu, D. Liu, H. Tang, G. Luo, K. Tu, Z. Z. Xie, J. Lei, J. Li, X. Li and D. Qu, *J. Appl. Electrochem.*, 2019, **49**, 1103–1112.

51 L. Wang, X. Zhu, K. Tu, D. Liu, H. Tang, J. Li, X. Li, Z. zhong Xie and D. Qu, *Electrochim. Acta*, 2020, 136726, DOI: **10.1016/j.electacta.2020.136726**.

52 Y. Wang, X. Zhu, D. Liu, H. Tang, G. Luo, K. Tu, Z. Z. Xie, J. Lei, J. Li, X. Li and D. Qu, *J. Appl. Electrochem.*, 2019, **49**, 1103–1112.

53 X. Li, Y. Li, X. Guo and Z. Jin, *Front. Chem. Sci. Eng.*, 2023, **17**, 606–616.

54 W. Zhang, C. Xu, E. Liu, J. Fan and X. Hu, *Appl. Surf. Sci.*, 2020, 146039, DOI: **10.1016/j.apsusc.2020.146039**.

55 K. Yang, Y. Zhang, C. Meng, F. F. Cao, X. Chen, X. Fu, W. Dai and C. Yu, *Appl. Surf. Sci.*, 2017, **391**, 635–644.

56 T. V. M. Sreekanth, R. Ramaraghavulu, S. V. Prabhakar Vattikuti, J. Shim and K. Yoo, *Mater. Lett.*, 2019, **253**, 450–453.

57 Y. Bi, H. Fan, C. Hu, R. Wang, L. Niu, G. Wen and L. Qin, *RSC Adv.*, 2024, **14**, 11734–11745.

58 H. Huang, J. Zhao, H. Guo, B. Weng, H. Zhang, R. A. Saha, M. Zhang, F. Lai, Y. Zhou, R. Z. Juan, P. C. Chen, S. Wang, J. A. Steele, F. Zhong, T. Liu, J. Hofkens, Y. M. Zheng, J. Long and M. B. J. Roeffaers, *Adv. Mater.*, 2024, 2313209, DOI: **10.1002/adma.202313209**.

59 X. Tang, M. Liang, Y. Zhang, W. Sun and Y. Wang, *Dalton Trans.*, 2019, **48**, 4413–4419.

60 N. T. M. Tho, B. T. Huy, D. N. N. Khanh, H. N. N. Ha, V. Q. Huy, N. T. T. Vy, D. M. Huy, D. P. Dat and N. T. K. Phuong, *Korean J. Chem. Eng.*, 2018, **35**, 2442–2451.

61 N. Sharma, Z. Pap, I. Székely, M. Focsan, G. Karacs, Z. Nemeth, S. Garg and K. Hernadi, *Appl. Surf. Sci.*, 2021, 150605, DOI: **10.1016/j.apsusc.2021.150605**.

62 E. M. S. Azzam, N. A. Fathy, S. M. El-Khouly and R. M. Sami, *J. Water Proc. Eng.*, 2019, **28**, 311–321.

63 Y. Huang, R. Li, D. Chen, X. Hu, P. Chen, Z. Chen and D. Li, *Catalysts*, 2018, 151, DOI: **10.3390/catal8040151**.

64 L. Tian, L. Ye, J. Liu and L. Zan, *Catal. Commun.*, 2012, **17**, 99–103.

65 B. T. Huy, D. S. Paeng, C. Thi Bich Thao, N. T. Kim Phuong and Y. I. Lee, *Arabian J. Chem.*, 2020, **13**, 3790–3800.

66 M. S. Khan, M. F. García, M. Javed, A. Kubacka, U. Caudillo-Flores, S. A. Halim, A. Khan, A. Al-Harrasi and N. Riaz, *ACS Omega*, 2021, **6**, 26108–26118.

67 V. D. Doan, T. T. N. Nguyen, H. A. Le Pham, T. L. H. Nguyen, O. E. Lebedeva, H. P. Dang, A. T. Nguyen, V. A. Tran and V. T. Le, *J. Mol. Liq.*, 2024, 124261, DOI: **10.1016/j.molliq.2024.124261**.

68 M. F. Hanafi and N. Sapawe, in *Materials Today: Proceedings*, Elsevier Ltd, 2020, vol. 31, pp. 318–320.

69 E. Hapeshi, I. Fotiou and D. Fatta-Kassinos, *Chem. Eng. J.*, 2013, **224**, 96–105.

70 Q. Wang, B. Wang, Y. Ma and S. Xing, *Chem. Eng. J.*, 2018, **354**, 473–480.

71 Q. Wang, P. Li, Z. Zhang, C. Jiang, K. Zuojiao, J. Liu and Y. Wang, *J. Photochem. Photobiol., A*, 2019, **378**, 114–124.

72 B. Weng, K. Q. Lu, Z. Tang, H. M. Chen and Y. J. Xu, *Nat. Commun.*, 2018, 1543, DOI: **10.1038/s41467-018-04020-2**.

73 I. Michael, E. Hapeshi, J. Aceña, S. Perez, M. Petrović, A. Zapata, D. Barceló, S. Malato and D. Fatta-Kassinos, *Sci. Total Environ.*, 2013, **461–462**, 39–48.

74 G. Zhao, J. Ding, F. Zhou, X. Chen, L. Wei, Q. Gao, K. Wang and Q. Zhao, *Chem. Eng. J.*, 2021, 126704, DOI: **10.1016/j.cej.2020.126704**.

75 H. Guo, Z. Li, S. Lin, D. Li, N. Jiang, H. Wang, J. Han and J. Li, *Chemosphere*, 2021, 129089, DOI: **10.1016/j.chemosphere.2020.129089**.

76 E. Hapeshi, I. Fotiou and D. Fatta-Kassinos, *Chem. Eng. J.*, 2013, **224**, 96–105.

77 Q. Wang, P. Li, Z. Zhang, C. Jiang, K. Zuojiao, J. Liu and Y. Wang, *J. Photochem. Photobiol., A*, 2019, **378**, 114–124.

78 Q. Wang, B. Wang, Y. Ma and S. Xing, *Chem. Eng. J.*, 2018, **354**, 473–480.

79 C. A. Lipinski, F. Lombardo, B. W. Dominy and P. J. Feeney, *Adv. Drug Delivery Rev.*, 2012, **64**, 4–17.